



Optical technology for arbitrarily manipulating amplitudes and phases of coaxially propagating highly discrete spectra

C. Zhang,¹ K. Yoshii,^{1,2} D. Tregubov,^{1,3} C. Ohae,^{2,4} J. Zheng,¹ M. Suzuki,^{1,4} K. Minoshima^{1,2,4} , and M. Katsuragawa^{1,2,4,*} 

¹Graduate School of Informatics and Engineering, University of Electro-Communications, 1-5-1 Chofugaoka, Chofu, Tokyo 182-8585, Japan

²JST, ERATO, MINOSHIMA Intelligent Optical Synthesizer Project, 1-5-1 Chofugaoka, Chofu, Tokyo 182-8585, Japan

³Optics Department, P. N. Lebedev Physical Institute of the Russian Academy of Sciences, Moscow 119991, Russia

⁴Institute for Advanced Science, University of Electro-Communications, 1-5-1 Chofugaoka, Chofu, Tokyo 182-8585, Japan



(Received 25 May 2019; published 18 November 2019)

The development of new optical technology plays a key role in the essential evolution of optical science. In this article, we experimentally demonstrate an optical technology that enables the arbitrary manipulation of amplitudes and phases of highly discrete spectra. This optical technology is simple and practically useful: we may only place a few fundamental optical elements on an optical axis and control their thicknesses precisely. As a typical application, we show generation of a train of ultrashort pulses in the time domain, with a pulse duration close to 1 fs and a repetition rate exceeding 100 THz.

DOI: [10.1103/PhysRevA.100.053836](https://doi.org/10.1103/PhysRevA.100.053836)

I. INTRODUCTION

The development of new optical technology paves the way for the essential evolution of optical science. The advent of chirped mirrors [1,2], which offered stable spectral dispersion control, enabled practical femtosecond lasers [3,4], and this matured femtosecond laser technology further opened attosecond science [5–7] through the generation of high harmonics. The invention of photonic crystal fibers [8,9] enabled the generation of a supercontinuum [10–12] with high spatial coherence, which subsequently opened the door to the optical frequency comb [13,14] through the control of the carrier envelope offset frequency. The optical frequency comb revolutionized optical frequency metrology [15,16], and its applicable scientific fields continue to expand.

Here, we report an optical technology that allows us to arbitrarily manipulate amplitudes and phases of highly discrete broad spectra. This technology is simple and practically useful; we may only place a few fundamental optical elements—a wave plate, a polarizer, and a transparent dispersive plate—on an optical axis and control their thicknesses precisely. As a typical application of this optical technology, we demonstrate the generation of a train of ultrashort pulses in the time domain, with a pulse duration of close to 1 fs and a repetition rate exceeding 100 THz. Such ultrahigh-repetition-rate ultrashort pulses may become a key tool for future ultrafast light-to-light information processing exceeding 100 THz.

First, we briefly explain some of the points in this study. The physical mechanism of this optical technology has been theoretically discussed [16,17] mainly on the basis of numerical calculations. In this article, we experimentally demonstrate that this technology can be practically operated. In principle, its physical mechanism includes random exploration over a wide parameter area [17,18]. Therefore, in addition to devel-

opment of a system for arbitrary manipulations of amplitude and phase, we developed a system for measurement of the amplitudes and spectral phases, including coupling of those functions as a whole system. One of the remarkable features of this technology is that these arbitrary manipulations can be performed without separating the broad spectra into their components in space. As imagined from recent intensive studies of coherent beam combining technology [19], such arbitrary amplitude and phase manipulations on a coaxial optical path should be advantageous for practically maintaining high beam quality and mutual coherence in time and space among the broad spectra.

II. CONCEPTUAL IDEA

Figure 1(a) shows a conceptual illustration of the arbitrary manipulation of amplitudes and phases of a highly discrete spectrum with a broad bandwidth. The geometric configuration is similar to the case of manipulating a single frequency, where a paired anisotropic crystal (wave plate in a broad sense) and a polarizer are used for manipulating its amplitude, and a transparent dispersive plate is used for manipulating its phase. The difference is that in manipulating multiple frequencies, we introduce precise controls on thicknesses of the optical elements over a wide range (typically several millimeters). The key physics discovered is that when the spectra are highly discrete (frequency spacing should be greater than tens of THz), we can frequently find good approximate solutions by simply sweeping their thicknesses even across a broad spectrum with an entire bandwidth of 1 PHz, if we abandon the idea of finding exact solutions [17,18].

Below, we briefly describe the physical mechanisms in these amplitude and phase manipulations. The laser power after the amplitude manipulation is given as

$$I_i(\Omega_i) = \cos^2 \left[\pi \frac{\Omega_i}{c} (n_e^{(i)} - n_o^{(i)}) \Delta d \right], \quad (1)$$

*katsuragawa@uec.ac.jp

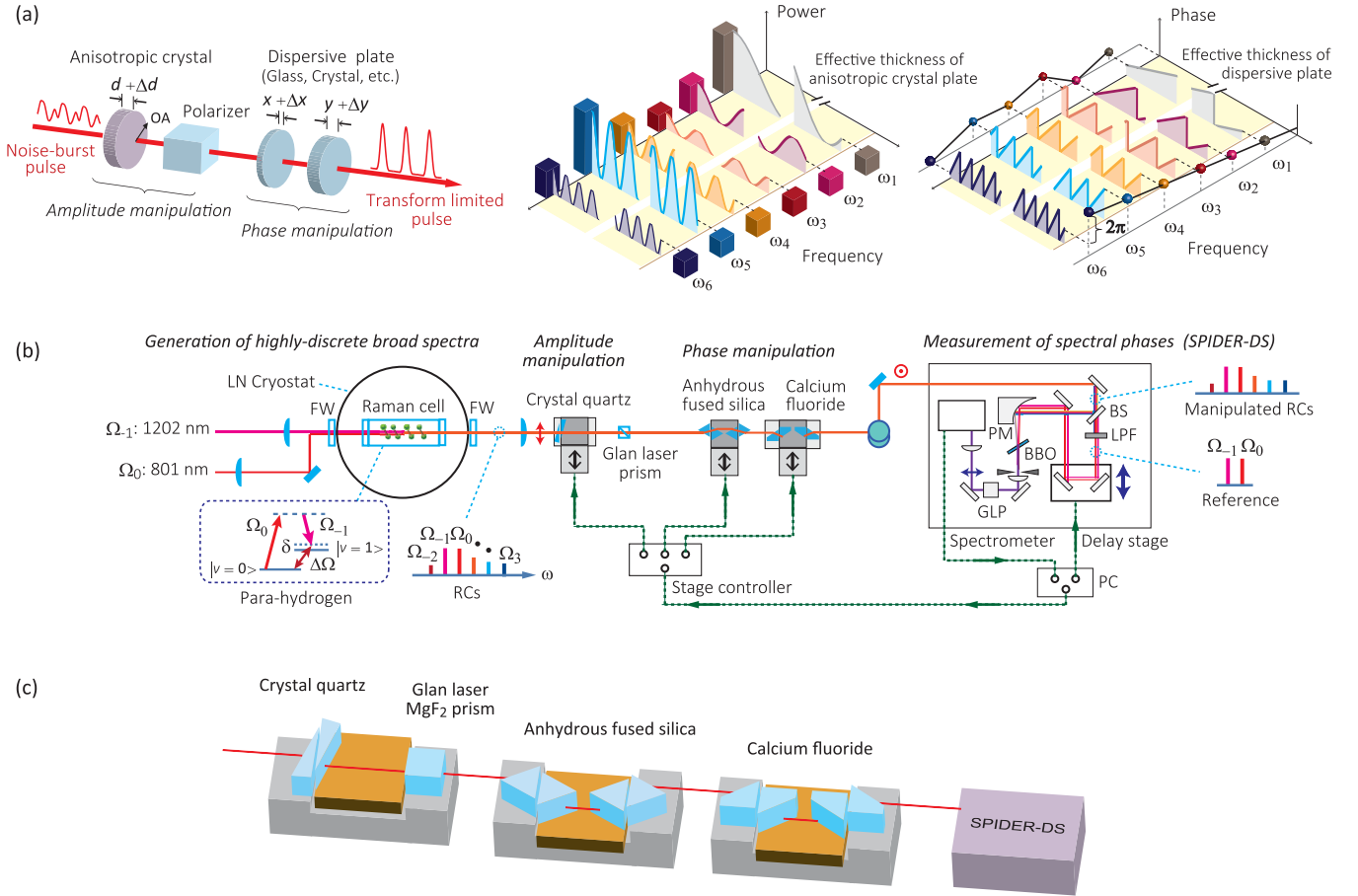


FIG. 1. Schematic of arbitrary manipulations of amplitudes and phases of a highly discrete broad spectrum. (a) Conceptual mechanism of arbitrary manipulation of amplitudes and phases. Variables indicate adjustable thicknesses of fundamental optical elements: $d + \Delta d$, wave plate; $x + \Delta x$, $y + \Delta y$, two kinds of dispersive plates. OA, optical axis. (b) Experimental setup, consisting of three partial systems: for generating highly discrete broad spectra, for arbitrarily manipulating amplitudes and spectral phases, and for measurement of spectral phases. Ω_{-2} to Ω_3 , frequencies of highly discrete spectra. LN, liquid nitrogen; FW, fused silica window; RCs, Raman components; PM, parabolic mirror; BS, beam splitter; LPF, long-wavelength pass filter; BBO, β -barium borate crystal; GLP, calcite Glan laser polarizer; PC, personal computer. (c) Detailed setups of the amplitude and phase manipulation devices.

where Ω_i is the frequency at the i th spectrum component; c is the speed of light in the vacuum; and $n_o^{(i)}$ and $n_e^{(i)}$ are refractive indices at the ordinary and extraordinary axes, respectively, of the anisotropic crystal plate at frequency Ω_i . As shown by Eq. (1), the output power, $I_i(\Omega_i)$, periodically oscillates as a function of thickness change of the anisotropic crystal plate, Δd . Given that the frequency spacing, $\Delta\Omega$, is very large, the oscillation period differs greatly depending on the spectrum component number, i . Thereby, we can realize a variety of power combinations among broad spectra, despite simply sweeping the crystal plate thickness, d . As a consequence, we frequently find good approximate solutions close to a desired power distribution among the broad spectra [18].

The physical mechanism of the phase manipulation is similar to that of the amplitude manipulation. The spectral phase after the phase manipulation is given as

$$\vartheta_i(\Omega_i) = \sum_k [\Phi_k \Delta L (i \Delta \Omega)^k], \quad (2)$$

where Φ_k denotes the coefficient of the k th-order dispersion and ΔL is the thickness change of the dispersive plate.

The spectral phase originating in the k th-order dispersion, $\Phi_k \Delta L (i \Delta \Omega)^k$, periodically oscillates as a function of the thickness change, ΔL . Since the broad spectra are highly discrete, the oscillation period differs greatly depending on the order, k . Therefore, we can realize a variety of weights of combinations among the high-order dispersion terms, implying a variety of spectral phases, $\vartheta_i(\Omega_i)$, for the broad spectra by simply scanning the thickness of the dispersive plate [18].

If we introduce another anisotropic crystal or dispersive plate made of a different material, we can greatly improve the capability in arbitrarily manipulating amplitudes or spectral phases, respectively [17,18]. Here, we demonstrate the generation of a train of ultrashort pulses in the time domain as a typical example of arbitrary manipulation of amplitudes and phases of a highly discrete spectrum. Manipulation of phase is generally more critical than that of amplitude when the purpose is the generation of optical wave forms in the time domain. So, we introduce an extended scheme using two kinds of dispersive plates for the phase manipulation, as illustrated in Fig. 1(a).

III. EXPERIMENT

Figure 1(b) presents a schematic of the experimental system. The system has three stages: generation of highly discrete broad spectra, arbitrary manipulation of their amplitudes and spectral phases, and measurement of the amplitude and phase distributions. We used a series of coherent vibrational Raman components (RCs) [20–25] with a frequency spacing of $\Delta\Omega = \Omega_0 - \Omega_{-1} = 124.7470$ THz as a highly discrete broad spectrum. The RCs were generated through adiabatic driving of a vibrational Raman coherence in gaseous para-hydrogen (density, 8×10^{19} cm⁻³; temperature, 77 K) by using a pair of driving lasers (Ω_{-1} , 1201.6350 nm; Ω_0 , 801.0820 nm) (for more details, see Appendix A). The above medium density and temperature were selected so that gaseous para-hydrogen was controlled to the Dicke regime [26], which provided the longest vibrational Raman coherence.

To arbitrarily manipulate amplitudes and phases of these RCs, we used a paired wedge-shaped crystal quartz (CQ) [27] and a calcite Glan laser polarizer for the amplitude manipulation, and two pairs of triangular-pole-shaped fused silica (FS) [28] and also two pairs of trapezoidal-pole-shaped calcium fluoride (CF) [29] for the phase manipulation [Fig. 1(c)]. CQ, FS, and CF were each separately installed on a translational stage, where a tiny gap of 10 μ m was precisely set for each pair of optical element blocks (see Appendix B). The translational stage precisely controlled the effective thickness of each optical element with a resolution of 0.1 μ m over a full scanning range of 20 mm, while the tiny gap of 10 μ m was maintained accurately.

The amplitudes of the RCs after the manipulation were simply measured by a power meter, and their spectral phases were determined by a spectral interferometry method specifically developed for highly discrete spectra [spectral phase interferometry for direct electric-field reconstruction for discrete spectra (SPIDER-DS)] [30,31] (for details, see Appendix C). As stated, the optical technology requires, in principle, random exploration over a wide thickness-parameter area. Therefore, we coupled the above two functions—i.e., the arbitrary amplitude and phase manipulations and their measurements and analysis in a variety of ways—to operate automatically as a complete system (for details, see Appendix B).

IV. RESULTS AND DISCUSSION

Figure 2(a) shows a photograph of the generated high-order RCs (Ω_{-1} : 1202 nm to Ω_3 : 401 nm); the white dotted circle indicates the Ω_{-2} (2403 nm) component, which cannot be detected with the camera used. All RCs were mutually phase coherent [32–35] and were generated coaxially without being restricted by the phase matching condition, which resulted in excellent Gaussian beam profiles. Figure 2(b) shows the observed power distribution of the six RCs. The original generated power of the second-order Stokes, Ω_{-2} , was low, while that of the first-order Stokes, Ω_{-1} , was high; the difference was spread over a wide range close to two orders of magnitude. Since our aim for arbitrary manipulation of amplitudes and spectral phases of the RCs was to generate ultrashort pulses in the time domain, we set the target for the amplitude manipulation to a near “flat” power distribution

[green bars in Fig. 2(d)], which simultaneously preserves their averaged power at the largest.

The practical difficulty in amplitude manipulation is that we cannot predict an optimal solution analytically, as this method is based on a random exploration of approximate solutions which are expected to appear frequently. Therefore, we have to experimentally explore near-optimal solutions over a wide range of the (CQ) crystal thickness, d , at high precision. To make this arbitrary amplitude manipulation more practical, we carried out this exploration as follows.

As shown in Eq. (1), each RC power oscillates periodically as a function of the CQ thickness. First, we tried to determine their periods experimentally, including the initial power distribution at $\Delta d = 0$, by sweeping the CQ thickness over a limited range of a few millimeters [initial sweeping; blue dotted lines in Fig. 2(c)].

Next, we fitted each of them with a sinusoidal function, then determined their periods, including the initial powers. The standard deviations (SDs) of the measured oscillating powers from the sinusoidal fitting curves were $<1\%$, and the differences of the estimated periods from those predicted by using the anisotropic refractive indices of the CQ were $<3\%$.

Third, on the basis of these estimated periods and initial powers, we numerically explored the power distributions over the entire possible range of CQ thicknesses. We occasionally found an optimal power distribution close to the target near the initial CQ thickness, $\Delta d = 0$ [red arrow in Fig. 2(c)].

Finally, according to the numerical prediction, we varied the CQ thickness around the red arrow, again measured power distributions precisely around it, and finally determined the optimal CQ thickness which gave the closest power distribution to the target. The red bars in Fig. 2(d) show the power distribution of the six RCs achieved in this way. The error bars indicate power fluctuations of the generated RCs, which were mainly created by shot-by-shot power fluctuation of the pair of driving lasers, Ω_{-1} and Ω_0 , used to adiabatically produce the vibrational Raman coherence. The power distribution achieved here matched the target well, with deviations from the target of $<10\%$. The gray bars in Fig. 2(d) represent the amplitude distribution normalized at Ω_{-1} , calculated from the red-bar power distribution.

Next, we describe the spectral phase manipulation. Phase manipulation is difficult in that we cannot predict an optimal solution analytically either, so we have to precisely explore a variety of thickness combinations of the two dispersive materials over a wide area of thickness parameters, including spectral interference measurement at each of the thickness parameters, to determine the spectral phases (for details of spectral phase measurement, see Appendix C). This is a much higher hurdle than that of amplitude manipulation, even though the phase manipulation, measurement, and data analysis were coupled and the whole system ran automatically. Below, we describe how we explored the optimal spectral phases.

First, we numerically investigated the behavior of the spectral phases over a sufficiently wide parameter area, varying the thickness combinations of FS and CF to identify the minimal parameter ranges required for finding at least one optimal solution [Fig. 3(a)]. As our aim was to produce ultrashort pulses in the time domain, to briefly represent the result of the

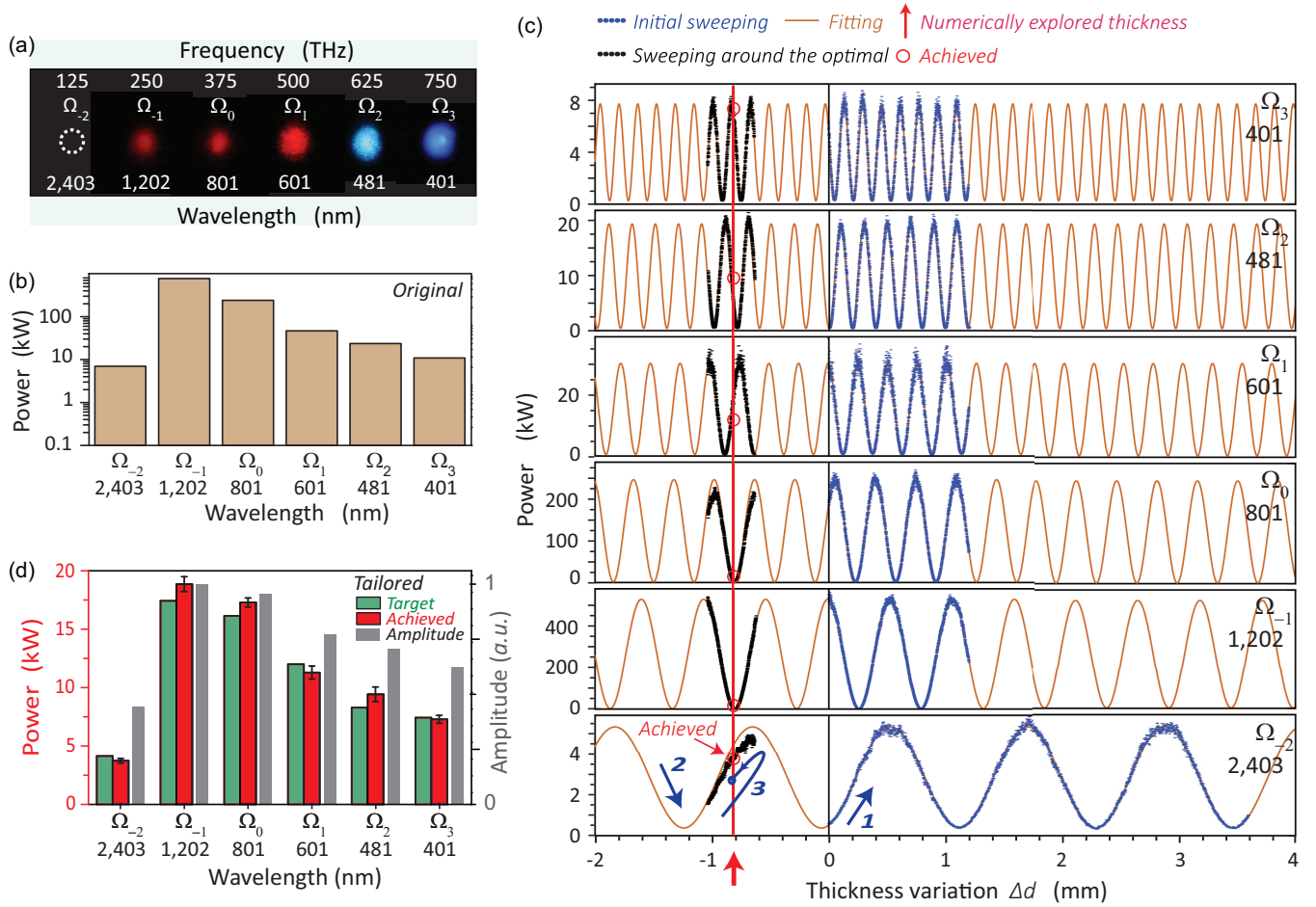


FIG. 2. Arbitrary manipulation of amplitudes of six high-order Raman components (RCs), Ω_{-2} to Ω_3 . (a) Photo of the generated high-order RCs. The RCs were separated in space by a Pellin-Broca prism. Their brightnesses, which covered a wide dynamic range, were adjusted with color filters. Then they were photographed individually with a silicon-sensor digital camera (that at Ω_{-2} , which this camera cannot detect, is circled). (b) Original power distribution of the six RCs: 7, 780, 240, 46, 24, and 11 kW for Ω_{-2} to Ω_3 , respectively. (c) Detail of arbitrary amplitude manipulation. Blue digits and arrows in “ Ω_{-2} ” indicate the manipulations: 1, initial scanning for determining the periods of the oscillating powers, including the initial powers; 2, fitting with sinusoidal functions to the oscillating powers observed in the initial scanning; 3, experimental exploration of optimal thickness around the numerically expected optimal thickness (-0.826 mm). (d) Tailored power and amplitude distributions. Green bars, target power distribution; red bars, power distribution experimentally achieved at the optimal thickness; gray bars, amplitude distribution normalized at that at Ω_{-1} , calculated from the achieved power distribution. Target power distributions were 4, 17, 16, 12, 8, and 7 kW for Ω_{-2} to Ω_3 , respectively; achieved power distributions were 4, 19, 17, 11, 9, and 7 kW for Ω_{-2} to Ω_3 , respectively. Error bars in red bars indicate power fluctuations in the RC generation process, which were in the range of $\pm 3\%$ to $\pm 7\%$ (SD).

phase manipulations, we contour-plotted the peak intensities of the temporal wave forms retrieved from the measured spectral phases. The peak intensities were normalized to that of the transform-limited waveform, TL; that is, unity (in red) corresponds to the target spectral phases (a linear phase relationship). As apparently indicated, the distribution of the peak intensities showed quasiperiodic variations. On the basis of this result, we determined the size of the area to be experimentally explored as that indicated by the white frame (0.2 mm \times 0.2 mm). Although it is difficult to exactly know the initial spectral phase in advance, we can expect to find at least one near-optimal solution if we completely explore it over this size of area.

Figure 3(b) shows an enlarged view of the area indicated by the white frame in Fig. 3(a). To confirm the reliability of this numerical prediction, we examined the spectral phase

manipulation and actual measurement of a parameter area of the same size as in Fig. 3(b). Figure 3(c) shows the result of a spectral phase manipulation with a relatively low thickness resolution of 0.01 mm (21×21 measurement points), as the purpose here is to determine the reliability of the calculation. As seen here, the measured spectral phases agreed well with the numerical prediction in Fig. 3(b).

On the basis of this ascertainment, we focused on the areas indicated by the white frame in Fig. 3(b), measuring 0.05 mm \times 0.05 mm [Fig. 3(d)]. Since we could restrict the area to a small enough size, we again experimentally examined the spectral phase manipulation while having a quadrupled thickness resolution of 0.0025 mm, which gave 21×21 measurement points in the focal area [Fig. 3(d)]. The result shows very good accordance with the prediction [Fig. 3(e)].

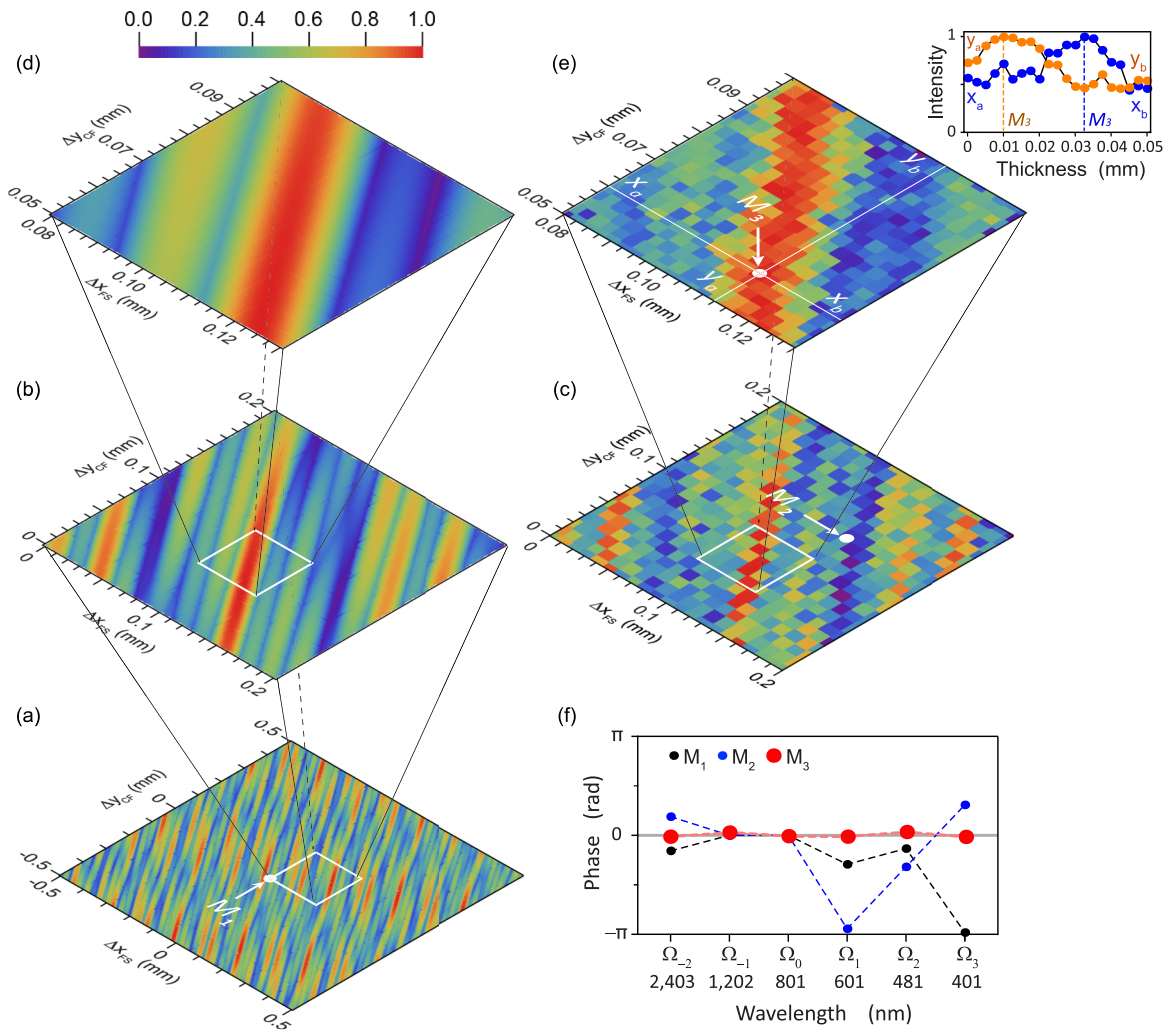


FIG. 3. Arbitrary manipulation of spectral phases of the six high-order RCs. (a) Contour plot of peak intensities of temporal wave forms retrieved from the spectral phases calculated numerically as functions of FS (Δx_{FS} , x axis) and CF (Δy_{CF} , y axis) thicknesses over a large area of $1 \text{ mm} \times 1 \text{ mm}$. The white frame indicates the minimal area size ($0.2 \text{ mm} \times 0.2 \text{ mm}$) to be explored. Point M_1 indicates the initial thickness combination determined experimentally. (b) Enlarged view of the parameter area indicated by the white frame ($0.05 \text{ mm} \times 0.05 \text{ mm}$) in (a). The white frame in (b) indicates the focus parameter area used to determine the optimal thickness combination. (c) Contour plot of peak intensities estimated by the measured spectral phases (thickness resolution of 0.01 mm , 21×21 measurement points) in the parameter area corresponding to (b). (d) Enlarged view of the parameter area indicated by the white frame in (b). (e) Contour plot of peak intensities estimated by the measured spectral phases (thickness resolution of 0.0025 mm , 21×21 measurement points) in the parameter area corresponding to (d). Point M_3 indicates the optimal thickness combination explored. The graph beside (e) plots the results picked up along the thickness changes, indicated by $x_a - x_b$ and $y_a - y_b$ in (e). The values of x_a and y_a are set to 0 to simplify the notation. (f) Spectral phases observed at the thickness combinations M_1 (initial thicknesses), M_2 (far from optimal), and M_3 (optimal thicknesses).

Finally, we experimentally determined the optimal thickness combination of the two dispersive plates, FS and CF, from the result of Fig. 3(e). The thickness combination indicated by M_3 provided the closest spectral phase to the target. The graph beside Fig. 3(e) plots the results of Fig. 3(e), picked up along the thickness changes of Δx_{FS} or Δy_{CF} , intersecting the point M_3 . We consider that the determined thickness combination at M_3 was optimal. Figure 3(f) represents the spectral phases of the six RCs (red circles) achieved at M_3 . All of the spectral phases were very close to 0 rad. For reference, we show the spectral phases at M_1 (black circles; initial thickness combination) and M_2 (blue circles; with a thickness combination far from the optimal, M_3).

From these tailored amplitudes and spectral phases, we finally retrieved the optical wave forms in the time domain [Fig. 4(a)]. At the optimal point, M_3 , a train of 1.4-fs ultrashort pulses (pink) was produced with a repetition rate of 124.7470 THz (pulse interval, 8.02 fs), which was our target. The peak intensity of the wave form reached 0.996, very close to that (i.e., 1) of the TL wave form (black). In contrast, at the thickness combination of the two dispersive plates, indicated by M_2 , the optical wave form was like noise burst pulses (blue). This shows that the optical wave forms were manipulated over a wide dynamic range with this optical technology, which arbitrarily manipulates amplitudes and spectral phases of highly discrete spectra.

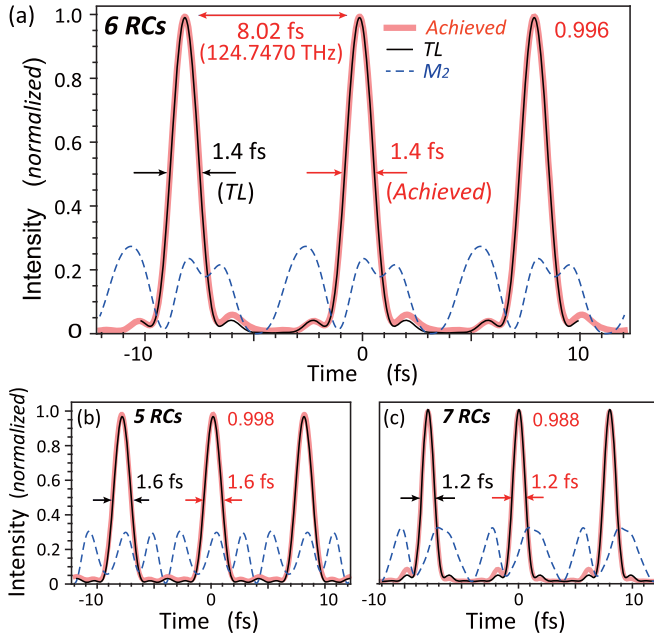


FIG. 4. Temporal wave forms retrieved from amplitudes and spectral phases of the six high-order RCs. (a) Temporal wave forms of RCs Ω_{-2} to Ω_3 . Thick pink lines, retrieved at the optimal point, M_3 ; thin black lines, assuming the transform-limited (TL) condition; dashed blue lines, at M_2 . The peak intensity of the wave form achieved at M_3 is 0.996, close to that (i.e., 1) of the TL condition. (b) Temporal wave forms for five high-order RCs, Ω_{-2} to Ω_2 . (c) Temporal wave forms for seven high-order RCs, Ω_{-2} to Ω_4 .

Note that this optical technology is applicable with an equivalent accuracy even for a broader bandwidth of ~ 1 PHz which, for example, consists of 12 RCs expanding over near-infrared, visible, and ultraviolet wavelength regions [17,18]. Figures 4(b) and 4(c) show other demonstrations of the arbitrary amplitude and phase manipulations for the cases of five RCs (2403–481 nm) and seven RCs (2403–343 nm), respectively, where, according to the full bandwidth determined by the number of the RCs, ultrashort pulses—1.6 fs and 1.2 fs, respectively—were produced in the time domain (for details, see Appendix D). The maximal spectral bandwidth that this optical technology can be applied to is currently limited by the maximum number of high-order Raman components (currently, seven components) which can be generated with a sufficient output power.

V. CONCLUSIONS

We have demonstrated an optical technology for arbitrarily manipulating amplitudes and phases of highly discrete broad spectra. The essence of the technology is simple: we place a few fundamental optical elements on the optical axis and precisely control their thicknesses. To make this technology work practically, we constituted it as a system that was composed of arbitrary manipulations of amplitude and phase; amplitude and spectral phase measurement of a highly discrete broad spectrum; and analysis of them, including coupling of those functions to run automatically, since this technology, in principle, requires random exploration over wide parameter ranges

regarding thickness of the optical elements. As a typical example, we applied it to a broad Raman spectrum with a highly discrete frequency spacing of 124.7470 THz, resulting in the generation of ultrashort pulses with a repetition rate of 124.7470 THz in the time domain (shortest pulse duration of 1.2 fs for the seven Raman components at 2403–343 nm).

The remarkable feature of this optical technology is that the manipulations are performed on a coaxial optical path without separating the broad spectra in space. Also, this technology is scalable to a high-power laser or a microscale system. Recently it has been reported that optical-field-induced current or dielectric response in solid materials can have ultrafast responses of attosecond timescales [36–38]. Our technology, including the above achievement—generation of ultrashort pulses with an ultrahigh repetition rate exceeding 100 THz—may become a key tool for future ultrafast light-to-light information processing.

ACKNOWLEDGMENTS

The authors thank Yusuke Furukawa for helpful discussions. This work is supported by a Grant-in-Aid for Scientific Research (A) (No. 24244065) and JST, ERATO MINOSHIMA Intelligent Optical Synthesizer Project (IOS) (JP-MJER1304).

APPENDIX A: ADIABATIC GENERATION OF HIGH-ORDER STIMULATED RAMAN SCATTERING COMPONENTS

We used gaseous para-hydrogen (purity $> 99.9\%$) as an interaction medium, which was installed in a copper Raman cell with an interaction length of 15 cm. The temperature of the Raman cell was set at that of liquid nitrogen, 77 K. The density of the para-hydrogen gas was controlled at $8 \times 10^{19} \text{ cm}^{-3}$, which provided the longest coherence time at 77 K. A pair of single-frequency nanosecond pulsed lasers (repetition rate: 10 THz) were used to adiabatically drive the vibrational Raman coherence ($v' = 1, J' = 0 \leftarrow v'' = 0, J'' = 0$). One was an injection-locked nanosecond pulsed Ti:sapphire laser (Ω_0) [39–41] with a wavelength of 801.0820 nm, an output energy of 6 mJ, and a pulse duration of 7 ns. The other was a single-frequency nanosecond laser (Ω_{-1}) realized via an injection-seeded optical parametric process, where the driving laser was the above injection-locked nanosecond pulsed Ti:sapphire laser, with a wavelength of 1201.6350 nm, an output energy of 6 mJ, and a pulse duration of 7 ns. The two-photon detuning [δ in Fig. 1(b)] to the vibrational Raman resonance was controlled to be optimal (-300 MHz) for adiabatically producing the highest vibrational Raman coherence. These two driving laser radiations were overlapped coaxially and were softly focused into the para-hydrogen gas. The estimated peak intensities in the interaction region were 180 MW/cm^2 for Ω_0 and 120 MW/cm^2 for Ω_{-1} .

APPENDIX B: AMPLITUDE AND PHASE MANIPULATION DEVICES

Each pair of optical elements was precisely installed with a tiny gap of $10 \mu\text{m}$ on the translational stages (Sigma

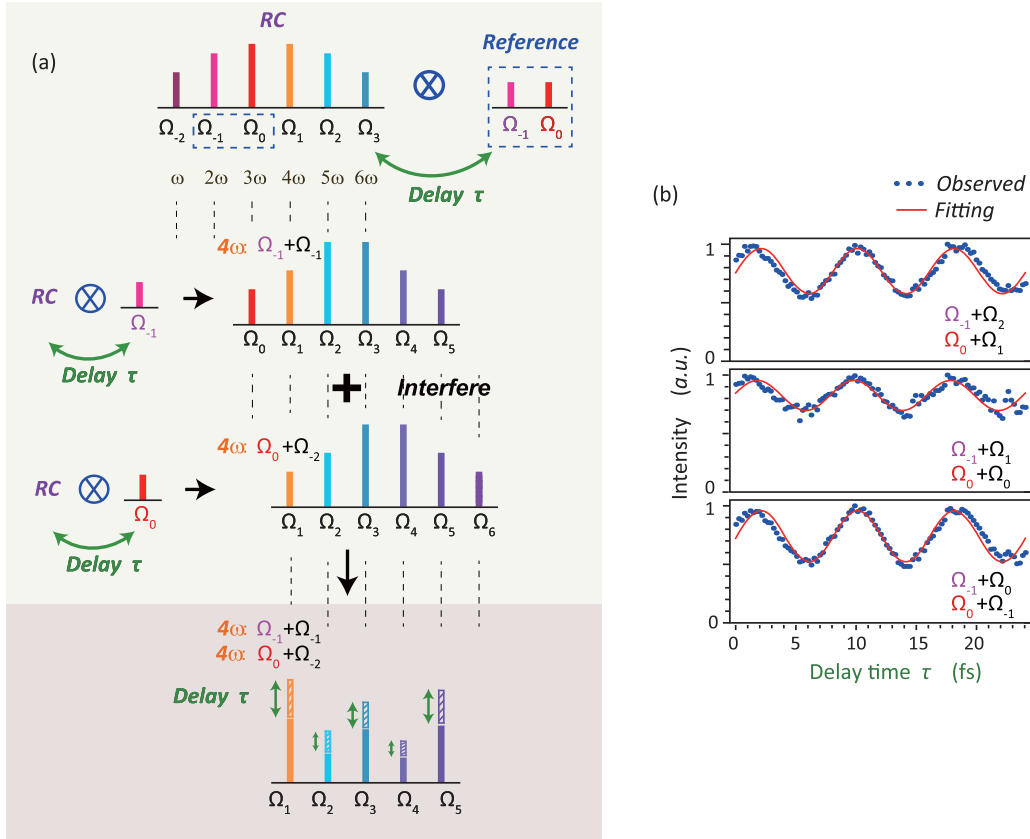


FIG. 5. Spectral phase interferometry for direct electric field reconstruction specifically designed for discrete spectra (SPIDER-DS). (a) Concept of SPIDER-DS. (b) A typical example of the interference spectral intensities, I_m , measured as a function of the time delay, τ .

Tech FS-1020X), achieved by the use of a tungsten wire of 10- μm diameter. The translational stages were controlled by a dedicated driver (Sigma Tech FC-101) connected to a PC and operated under the control of LabVIEW software. We tested the basic performance of these optical devices in advance and ascertained that the effective thickness resolution was better than 0.1 μm and was maintained over the whole translational range of 20 mm by keeping a tiny gap of 10 μm .

APPENDIX C: SPECTRAL PHASE INTERFEROMETRY FOR DIRECT ELECTRIC FIELD RECONSTRUCTION FOR DISCRETE SPECTRA (SPIDER-DS)

The spectral phase measurement was performed by using a specifically developed method, in which the essential idea of SPIDER—spectral interference between two kinds of replicas of the original spectrum—was extended so that it can be applicable to discrete spectra (RCs). As illustrated in Fig. 5(a), the two kinds of replicas of the original discrete spectra, with the same frequency shift as the frequency spacing, $\Delta\Omega$, of the replica spectra, were produced by mixing the original spectra (Ω_{-2} to Ω_3) with a pair of single frequencies (Ω_{-1} and Ω_0 : the reference) which were picked up from the original spectra themselves:

$$\begin{aligned} I_m &= |E_{m-1}E_0^R e^{i\Omega_0\tau} + E_mE_{-1}^R e^{i\Omega_{-1}\tau}|^2 \\ &= |E_{m-1}E_0^R|^2 + |E_mE_{-1}^R|^2 \end{aligned}$$

$$\begin{aligned} &+ 2|E_{m-1}E_mE_0^R E_{-1}^R| \cos[\Delta\Omega\tau - (\varphi_m - \varphi_{m-1}) \\ &+ (\varphi_0^R - \varphi_{-1}^R)]. \end{aligned} \quad (\text{C1})$$

The two replica spectra were phase coherent with each other and perfectly overlapped in the frequency domain. Thereby, the spectral interference was created. Equation (C1) quantitatively describes this spectral interference. Here $E_m = |E_m|e^{i\varphi_m}$ is the complex electric-field amplitude, m is an integer number, superscript R implies the physical quantities regarding the reference, and τ is a time delay of the reference against the original spectra. As implied by Eq. (C1), the interference spectral intensities, I_m , oscillate periodically as a function of the time delay, τ . Figure 5(b) shows such typical behaviors of I_m measured here. The relative phase between the references, $\varphi_0^R - \varphi_{-1}^R$, is common for all the I_m . Therefore, regardless of the value of $\varphi_0^R - \varphi_{-1}^R$, the relative spectral phase, $\varphi_m - \varphi_{m-1}$, between the spectral components, Ω_m and Ω_{m-1} , can be deduced from the measured periodic oscillations of I_m as a function of τ . The spectral phases of the original spectra (Ω_{-2} to Ω_3 : RCs) were determined one by one in this way.

The optical technology requires that the phase measurement system quickly estimate the spectral phases of broad spectra and analyze the results rapidly to display them on a PC monitor in a variety of ways depending on the purpose of the amplitude and phase manipulations. All of these processes must be performed automatically.

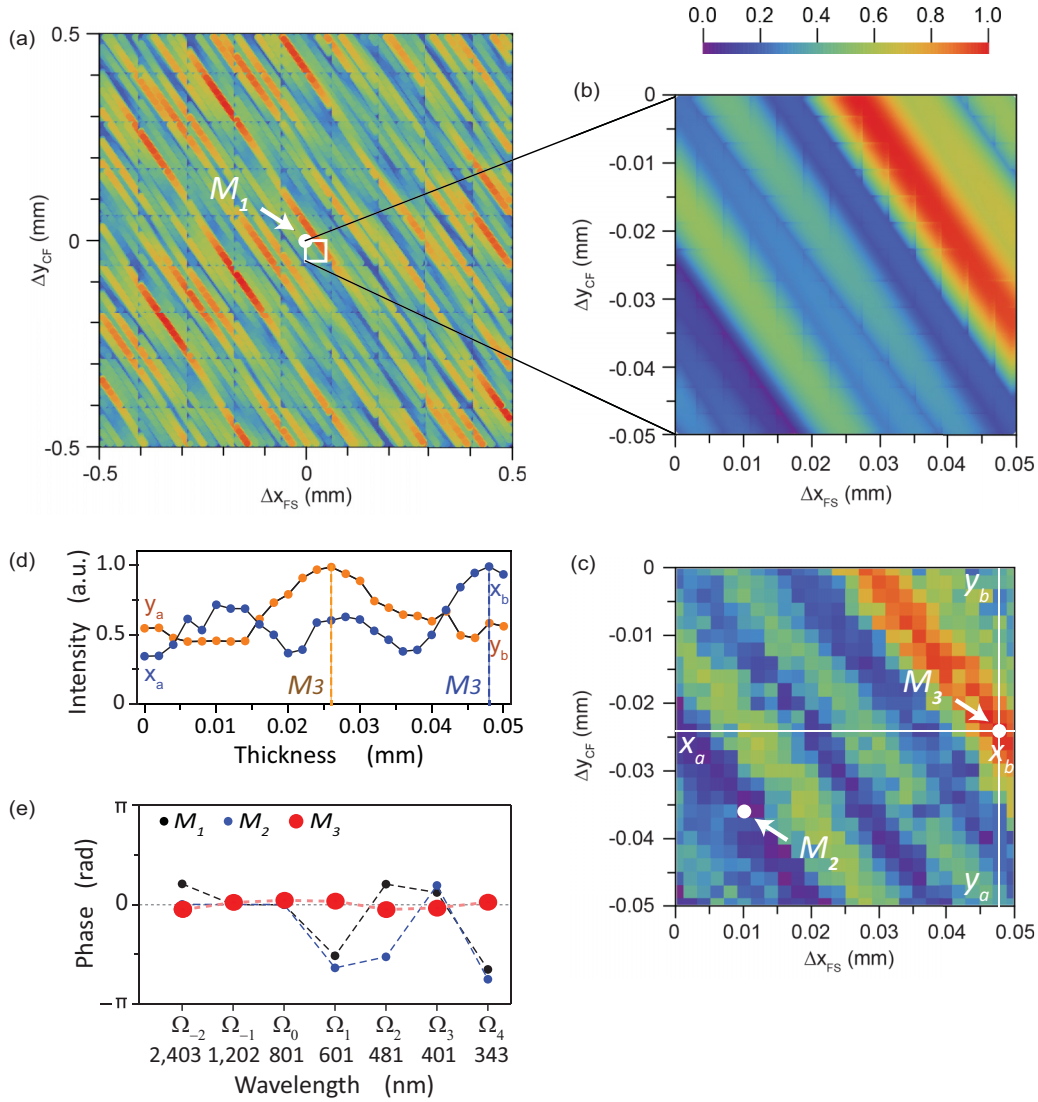


FIG. 6. Arbitrary manipulation of spectral phases of seven high-order RCs. (a) Contour plot of peak intensities of temporal wave forms retrieved from the spectral phases calculated numerically as functions of FS (Δx_{FS}) and CF (Δy_{CF}) thicknesses over a large area of 1 mm \times 1 mm. The white frame indicates the focal parameter area (0.05 mm \times 0.05 mm) to determine the optimal thickness combination. Point M_1 indicates the initial thickness combination determined experimentally. (b) Enlarged view of the parameter area indicated by the white frame in (a). (c) Contour plot of peak intensities estimated by the measured spectral phases (thickness resolution of 0.0025 mm, 21 \times 21 measurement points) in the area corresponding to (b). Point M_3 indicates an optimal thickness combination explored experimentally. (d) The graph plots the results picked up along the thickness changes, indicated by $x_a - x_b$ and $y_a - y_b$ in (c). The values at x_a and y_a are set as 0 to simplify the notation. (e) Spectral phases observed at the thickness combinations M_1 (initial thicknesses), M_2 (far from optimal), and M_3 (optimal thicknesses).

The SPIDER-DS satisfied these requirements well. The conceptual layout of the SPIDER-DS is illustrated in Fig. 1(b) in the main text. The incident beam (original spectrum) to be measured is separated into two beams by a glass plate, where the incident partial power is transmitted, and only the frequency components, Ω_{-1} and Ω_0 , are extracted by a long-wavelength pass filter (LPF) as the reference. After an appropriate time delay, τ , is added to the reference beam, the beam is focused with a parabolic mirror onto a 10- μ m-thick β -barium-borate (BBO) crystal together with the original spectral beam. The sum frequencies of the original spectrum and the reference are generated at the BBO thin crystal (type-I phase matching), and are finally introduced into a spectrom-

eter (Ocean Optics USB4000; acceptable wavelength range, 200–1100 nm) to measure I_m as a function of τ . The delay stage is needed to have a relatively high positional resolution over a long translational range, the required specification of which depends on the frequency spacing, $\Delta\Omega$. We used a translational stage (nPoint Inc., nPoint LC 400) with a positional resolution of < 1 nm over the full translational range of 100 μ m. The I_m signals obtained in the spectrometer were sent to a PC operated under the control of LabVIEW software and processed there together with the amplitude manipulation signals to display them rapidly in a variety of ways on a PC monitor and to feed them back to the amplitude or spectral phase manipulation systems depending on the purposes.

APPENDIX D: ARBITRARY MANIPULATION OF SPECTRAL PHASES OF SEVEN HIGH-ORDER RCs

The arbitrary manipulation is shown in Fig. 6.

-
- [1] R. Szipocs, K. Ferencz, C. Spielmann, and F. Krausz, Chirped multilayer coatings for broadband dispersion control in femtosecond lasers, *Opt. Lett.* **19**, 201 (1994).
- [2] F. X. Kärtner, N. Matuschek, T. Schibli, U. Keller, H. A. Haus, C. Heine, R. Morf, V. Scheuer, M. Tilsch, and T. Tschudi, Design and fabrication of double-chirped mirrors, *Opt. Lett.* **22**, 831 (1997).
- [3] A. Stingl, M. Lenzner, C. Spielmann, F. Krausz, and R. Szipocs, Sub-10-fs mirror-dispersion-controlled Ti:sapphire laser, *Opt. Lett.* **20**, 602 (1995).
- [4] L. Gallmann, D. H. Sutter, N. Matuschek, G. Steinmeyer, U. Keller, C. Iaconis, and I. A. Walmsley, Characterization of sub-6-fs optical pulses with spectral phase interferometry for direct electric-field reconstruction, *Opt. Lett.* **24**, 1314 (1999).
- [5] M. Hentschel, R. Kienberger, C. Spielmann, G. A. Reider, N. Milosevic, T. Brabec, P. Corkum, U. Heinzmann, M. Drescher, and F. Krausz, Attosecond metrology, *Nature (London)* **414**, 509 (2001).
- [6] F. Krausz and M. Ivanov, Attosecond physics, *Rev. Mod. Phys.* **81**, 163 (2009).
- [7] F. Krausz and M. K. Stockman, Attosecond metrology: From electron capture to future signal processing, *Nat. Photonics* **8**, 205 (2014).
- [8] T. A. Birks, J. C. Knight, and P. S. J. Russell, Endlessly single-mode photonic crystal fiber, *Opt. Lett.* **22**, 961 (1997).
- [9] J. K. Ranka, R. S. Windeler, and A. J. Stentz, Visible continuum generation in air-silica microstructure optical fibers with anomalous dispersion at 800 nm, *Opt. Lett.* **25**, 25 (2000).
- [10] T. A. Birks, W. J. Wadsworth, and P. S. J. Russell, Supercontinuum generation in tapered fibers, *Opt. Lett.* **25**, 1415 (2000).
- [11] J. M. Dudley, G. Genty, and S. Coen, Supercontinuum generation in photonic crystal fiber, *Rev. Mod. Phys.* **78**, 1135 (2006).
- [12] F. Belli, A. Abdolvand, W. Chang, J. C. Travers, and P. S. J. Russell, Vacuum-UV to IR supercontinuum in hydrogen-filled photonic crystal fiber, *Optica* **2**, 292 (2015).
- [13] T. Udem, J. Reichert, R. Holzwarth, and T. W. Hänsch, Absolute Optical Frequency Measurement of the Cesium D_1 Line with a Mode-Locked Laser, *Phys. Rev. Lett.* **82**, 3568 (1999).
- [14] D. J. Jones, S. A. Diddams, J. K. Ranka, A. Stentz, R. S. Windeler, J. L. Hall, and S. T. Cundiff, Carrier-envelope phase control of femtosecond mode-locked lasers and direct optical frequency synthesis, *Science* **288**, 635 (2000).
- [15] T. Udem, R. Holzwarth, and T. W. Hänsch, Optical frequency metrology, *Nature (London)* **416**, 233 (2002).
- [16] R. Holzwarth, T. Udem, T. W. Hänsch, J. C. Knight, W. J. Wadsworth, and P. S. J. Russell, Optical Frequency Synthesizer for Precision Spectroscopy, *Phys. Rev. Lett.* **85**, 2264 (2000).
- [17] K. Yoshii, J. K. Anthony, and M. Katsuragawa, The simplest route to generating a train of attosecond pulses, *Light: Sci. Appl.* **2**, e58 (2013).
- [18] M. Katsuragawa and K. Yoshii, Arbitrary manipulation of amplitude and phase of a set of highly discrete coherent spectra, *Phys. Rev. A* **95**, 033846 (2017).
- [19] A. Klenke, M. Müller, H. Stark, M. Kienel, C. Jauregui, A. Tünnermann, and J. Limpert, Coherent beam combination of ultrafast fiber lasers, *IEEE J. Sel. Top. Quantum Electron.* **24**, 0902709 (2018).
- [20] S. E. Harris and A. V. Sokolov, Broadband spectral generation with refractive index control, *Phys. Rev. A* **55**, R4019 (1997).
- [21] A. V. Sokolov, D. R. Walker, D. D. Yavuz, G. Y. Yin, and S. E. Harris, Raman Generation by Phased and Antiphased Molecular States, *Phys. Rev. Lett.* **85**, 562 (2000).
- [22] J. Q. Liang, M. Katsuragawa, F. Le Kien, and K. Hakuta, Sideband Generation Using Strongly Driven Raman Coherence in Solid Hydrogen, *Phys. Rev. Lett.* **85**, 2474 (2000).
- [23] F. Couny, F. Benabid, P. J. Roberts, P. S. Light, and M. G. Raymer, Generation and photonic guidance of multi-octave optical-frequency combs, *Science* **318**, 1118 (2007).
- [24] F. C. Turner, A. Trotter, L. L. Losev, and D. Strickland, Transient multi-frequency Raman generation in SF₆, *Opt. Commun.* **270**, 419 (2007).
- [25] S. Baker, I. A. Walmsley, J. W. G. Tisch, and J. P. Marangos, Femtosecond to attosecond light pulses from a molecular modulator, *Nat. Photonics* **5**, 664 (2011).
- [26] K. Morimune, Master's thesis, University of Electro-Communications, 2017.
- [27] G. Ghosh, Dispersion-equation coefficients for the refractive index and birefringence of calcite and quartz crystals, *Opt. Commun.* **163**, 95 (1999).
- [28] I. H. Malitson, Interspecimen comparison of the refractive index of fused silica, *J. Opt. Soc. Am.* **55**, 1205 (1965).
- [29] M. Daimon and A. Masumura, High-accuracy measurements of the refractive index and its temperature coefficient of calcium fluoride in a wide wavelength range from 138 to 2326 nm, *Appl. Opt.* **41**, 5275 (2002).
- [30] I. A. Walmsley and V. Wong, Characterization of the electric field of ultrashort optical pulses, *J. Opt. Soc. Am. B* **13**, 2453 (1996).
- [31] T. Suzuki, N. Sawayama, and M. Katsuragawa, Spectral phase measurements for broad Raman sidebands by using spectral interferometry, *Opt. Lett.* **33**, 2809 (2008).
- [32] A. V. Sokolov, D. R. Walker, D. D. Yavuz, G. Y. Yin, and S. E. Harris, Femtosecond Light Source for Phase-Controlled Multiphoton Ionization, *Phys. Rev. Lett.* **87**, 033402 (2001).
- [33] M. Katsuragawa, K. Yokoyama, T. Onose, and K. Misawa, Generation of a 10.6-THz ultrahigh-repetition-rate train by synthesizing phase-coherent Raman-sidebands, *Opt. Express* **13**, 5628 (2005).
- [34] M. Y. Shverdin, D. R. Walker, D. D. Yavuz, G. Y. Yin, and S. E. Harris, Generation of a Single-Cycle Optical Pulse, *Phys. Rev. Lett.* **94**, 033904 (2005).

- [35] H. S. Chan, Z. M. Hsieh, W. H. Liang, A. H. Kung, C. K. Lee, C. J. Lai, R. P. Pan, and L. H. Peng, Synthesis and measurement of ultrafast waveforms from five discrete optical harmonics, *Science* **331**, 1165 (2011).
- [36] A. Schiffrin, T. P. Colberg, N. Karpowicz, V. Apalkov, D. Gerster, S. Mühlbrandt, M. Korbman, J. Reichert, M. Schultze, S. Holzner, J. V. Barth, R. Kienberger, R. Ernstorfer, V. S. Yakovlev, M. I. Stockman, and F. Krausz, Optical-field-induced current in dielectrics, *Nature (London)* **493**, 70 (2013).
- [37] M. Schultze, E. M. Bothschafter, A. Sommer, S. Holzner, W. Schweinberger, M. Fiess, M. Hofstetter, R. Kienberger, V. Apalkov, V. S. Yakovlev, M. I. Stockman, and F. Krausz, Controlling dielectrics with the electric field of light, *Nature (London)* **493**, 75 (2013).
- [38] T. Higuchi, C. Heide, K. Ullmann, H. B. Weber, and P. Hommelhoff, Light-field-driven currents in graphene, *Nature (London)* **550**, 224 (2017).
- [39] M. Katsuragawa and T. Onose, Dual-wavelength injection-locked pulsed laser, *Opt. Lett.* **30**, 2421 (2005).
- [40] T. Onose and M. Katsuragawa, Dual-wavelength injection-locked, pulsed laser with precisely predictable performance, *Opt. Express.* **15**, 1600 (2007).
- [41] T. Nakano, K. Koizumi, T. Onose, K. Abe, and M. Katsuragawa, Dual-frequency injection-locked nanosecond pulsed laser with arbitrary combination of two oscillation frequencies, *Opt. Express.* **18**, 26409 (2010).